



Uncertainty quantification and aerodynamic robust optimization of turbomachinery based on graph learning methods



Jinxing Li ^a, Tianyuan Liu ^{c,d}, Guangya Zhu ^b, Yunzhu Li ^a, Yonghui Xie ^{a,*}

^a State Key Laboratory for Strength and Vibration of Mechanical Structures, School of Energy and Power Engineering, Xi'an Jiaotong University, Xi'an, Shaanxi Province, 710049, China

^b MOE Key Laboratory of Thermo-Fluid Science and Engineering, School of Energy and Power Engineering, Xi'an Jiaotong University, Xi'an, Shaanxi Province, 710049, China

^c Engineering College, Peking University, Beijing, 100091, China

^d Baidu Online Network Technology (Beijing) Co., Ltd, Beijing, China

ARTICLE INFO

Handling Editor: L Luo

Keywords:

Uncertainty quantification
Aerodynamic robust optimization
Turbomachinery
Field prediction
Graph neural network

ABSTRACT

The actual operation of turbomachinery is inevitably affected by multi-source uncertainties. Such uncertainties are detrimental to the performance and reliability of energy systems. Based on graph learning methods, this work aims to provide a convenient and effective approach for aerodynamic robust optimization of turbomachinery. A radial inflow turbine is taken as the research target and Dual Graph Neural Network (DGNN) regression model is constructed for flow field prediction and performance discrimination. By comparing the accuracy and time consumption, the advantages of DGNN over classical surrogate models and computational fluid dynamics (CFD) are clarified. The proposed model is integrated into uncertainty quantification and aerodynamic robust optimization. The effect of multi-source uncertainties on performance is quantified. The stochastic response of flow fields is also obtained conveniently through DGNN. Robust optimization is performed for power and efficiency, respectively. The power robust optimization improves the power by 1.52% and reduces the standard deviation of power by 15.45%. The efficiency robust optimization achieves an efficiency improvement of 1.76% (increment) and an efficiency standard deviation reduction of 36.82%. The proposed approach is an efficient and competitive choice for uncertainty quantification and robust optimization. The present work contributes to constructing the digital twin of turbomachinery systems.

1. Introduction

As the core components of the energy conversion system, turbomachinery such as the compressor and turbine directly affect the energy conversion efficiency and system safety. Over the past few decades, many efforts have been devoted to improving the performance of turbomachinery, and significant achievements have been achieved [1, 2]. However, due to manufacturing error, operation condition fluctuation, and in-service degradation, no turbomachinery operates exactly at nominal design geometry or nominal conditions. Such uncertainties are usually detrimental and may cause the performance to deviate from the theoretically optimal solution. With the increasing requirements for the reliability of turbomachinery, the uncertainty quantification (UQ) of performance and aerodynamic robust optimization (ARO) have received increasing attention.

UQ aims to obtain the distribution characteristics of turbomachinery performance, identify the key uncertain parameters with important impacts, and provide guidance for geometry design, manufacturing, operation, and maintenance. A series of UQ studies have been reported for turbomachinery [3,4]. Schnell et al. [5] employed Monte Carlo (MC) simulation to obtain the aerodynamic response of a contrarotating turbofan to geometric variations. By coupling numerical simulations with a non-intrusive probabilistic collocation method, Liu et al. [6] analyzed the aerodynamic performance of wind turbines under stochastic boundary conditions. Razaaly et al. [7] investigated the effects of multi-source uncertainties on a supersonic turbine cascade with the help of a Kriging-based surrogated model and MC method. Wang et al. [8] used a polynomial chaos expansion-based Kriging surrogate model to quantify the geometric variations in the turbine aerodynamic performance. Xia et al. [9] proposed an adaptive sparse grid-based

* Corresponding author.

E-mail address: yhxie@mail.xjtu.edu.cn (Y. Xie).

non-intrusive polynomial chaos (NIPC) method to quantify the effect of pressure fluctuations on the aerodynamic performance of NASA Rotor 67. The uncertain response of flow fields was analyzed by MC simulation.

Based on the quantitative results, the ARO of turbomachinery aims to improve the average performance under uncertainties and decrease the sensitivity [10,11]. By combining response surface methodology, MC method, and a stochastic optimization algorithm, Javed et al. [12] performed the aerodynamic optimization of a centrifugal compressor impeller under manufacturing uncertainties. Tang et al. [13] optimized the aerodynamic robustness of a centrifugal compressor impeller under stochastic operation conditions by the generic algorithm and Kriging model. The uncertain response of the sample points for constructing the surrogate model was obtained by the NIPC method. Ju et al. [14] analyzed the response of a centrifugal compressor impeller to real manufacturing uncertainties by combining a bi-fidelity metamodel and MC method. The robustness of the impeller is improved by a sequential infilling sampling-based optimization method.

Performing UQ and ARO could be an expensive, laborious, and time-consuming task due to the enormous computational resource required for quantifying uncertainties. In this scenario, surrogate models are introduced as a low-cost alternative to the expensive high-fidelity analysis. Surrogate models have been successfully employed in various aspects of turbomachinery, such as performance prediction [15,16], design optimization [17,18], operation characteristic analysis [19,20], UQ [7,8,21], and ARO [10,12–14]. However, the actual uncertain inputs for turbomachinery include multiple source parameters (geometric and operating condition parameters), and the uncertain response includes multiple outputs. The aerodynamic robust optimization process further involves input design parameters. The computational demand for surrogate models exponentially increases with the dimension of the problem. “The curse of dimensionality” [22] increases the difficulty of constructing high-precision surrogate models. Therefore, comprehensive studies on ARO with multi-source uncertain inputs are challenging. Meanwhile, the flow field inside the turbomachinery is difficult for classical surrogate models due to its ultra-high-dimensional, strong nonlinearity, and spatial-temporal coupling characteristics. As a result, classical surrogate models tend to map the input design parameters directly to the performance parameters. This completely ignores the flow field information and lacks physical mechanism interpretability.

Recently, deep learning techniques have shown tremendous benefits in data-driven analysis in many industrial areas [23–25]. Deep learning techniques offer the potential to build digital twins [26] that respond to physical problems in seconds or even milliseconds. Inspired by the excellent performance of deep learning methods in image recognition, scholars have attempted to employ them in physical field regression. There have been some successful reports on the regression of steady [27, 28] and unsteady flow fields [29,30], temperature fields [31], and stress fields [32,33]. Han [34] adopted a convolutional neural network (CNN) and a Long Short Term Memory network to predict the fields around a cylinder and an airfoil. Sekar et al. [35] combined a CNN and a multi-layer perceptron to predict the 2D flow field around airfoils. Kashefi et al. [36] proposed a framework that directly uses the spatial coordinates information of computational fluid dynamics (CFD) grids to characterize flow fields. The proposed network achieved good results in the prediction of 2D flow fields around irregular geometries. Wang et al. [37] predicted the 1D flow field on the turbine surface and the turbine performance with the assistance of CNN.

So far, most of the research on physical field prediction adopted CNNs, which have been proven to be a promising deep learning category to predict physical fields. However, CNNs were proposed to deal with Euclidean data. The main criticism of CNNs is that they cannot be directly applied to physical fields defined on numerical simulation grids. Pixelation methods are required for most CNNs to convert the field data into fixed-size cartesian grids (Euclidean data), which undoubtedly introduces pixelation errors and limits the application of CNNs to complex

physical fields. Lately, extending deep learning methods for non-Euclidean graph data (so-called graph learning) has received increasing attention, and many graph neural networks (GNNs) [38] have been proposed to process non-Euclidean graph data. The physical field information defined on an arbitrary simulation grid can be considered as a kind of graph data, which may be irregular, out of order, and without a fixed number of neighboring nodes. Although GNNs have been successfully applied to many fields, including traffic networks [39], molecular geometry prediction [40], and recommendation systems [41], little attention has been paid to the application to physical field regression [42]. Sanchez-Gonzalez et al. [43] applied GNNs to the physical systems with particles to simulate the challenging physical motions. Pfaff et al. [44] proposed a framework for regression of simulation results on unstructured mesh, which realized accurate prediction of classical CFD problems such as cylinder flow and airfoil flow. Xu et al. [45] predicted the 2D flow field of the NACA0012 airfoil with the help of GNNs. Our previous work [46] first introduced GNN model into the aerodynamic analysis of turbomachinery, which can accurately predict the flow fields and aerodynamic performance.

The present study aims to provide a high-precision, rapid, and physical mechanism interpretable procedure for UQ and ARO of turbomachinery. Based on the concept of GNNs, a comprehensive dual graph neural network (DGNN) is designed for flow field prediction and performance discrimination. With the assistance of such a graph learning model, the UQ with multi-source uncertain inputs and ARO are performed for a radial inflow turbine impeller. The main contributions are as follows:

This is the first attempt to apply the graph deep learning method to assist the uncertainty qualification and robust optimization of turbomachinery. Nonlinear mappings of design variables, multi-source uncertainties to flow fields, and then to turbine performance are constructed. The non-Euclidean flow field data at CFD grids can be directly used for training and prediction. The network architecture and the processing of flow field data are illustrated in detail.

Through DGNN, the flow fields and aerodynamic performance can be obtained quickly and accurately. The performance of DGNN under different training sizes is analyzed in detail. The superiority of our model over classical surrogate models and CFD is clarified through the prediction accuracy and speed.

A combination of the DGNN model and MC method is used to quantify the stochastic response characteristics of the turbine. The effect of multi-source uncertainties on turbine performance is evaluated. The stochastic response of flow fields can also be obtained conveniently by the proposed graph learning method. Multi-objective optimizations are performed by NSGA-II, and turbines with excellent performance and robustness are obtained.

2. Methodology

The purpose of this work is to provide a new surrogate model for uncertainty qualification and robust optimization of turbomachinery, so as to solve the shortcomings of classical surrogate models, such as low accuracy and lack of physical mechanism interpretability. The surrogate model is constructed under the framework of GNNs. A framework for aerodynamic robust optimization of turbomachinery, referred to as DGNN-ARO, is developed based on the novel surrogate model. The overall workflow of the framework is shown in Fig. 1.

The framework consists of four sub-steps. Firstly, the parameterization of the research object (turbine impeller in this work) is conducted, and the design space and uncertain variables space are determined. The Latin hypercube sampling (LHS) method is adopted to generate the initial samples, and the network training dataset is obtained by the subsequent CFD calculation and post-processing. Secondly, based on the data-driven graph learning methods, the DGNN is constructed and trained with the dataset. A well-trained DGNN enables accurate prediction of flow fields and performance in nearly real-time. Afterward,

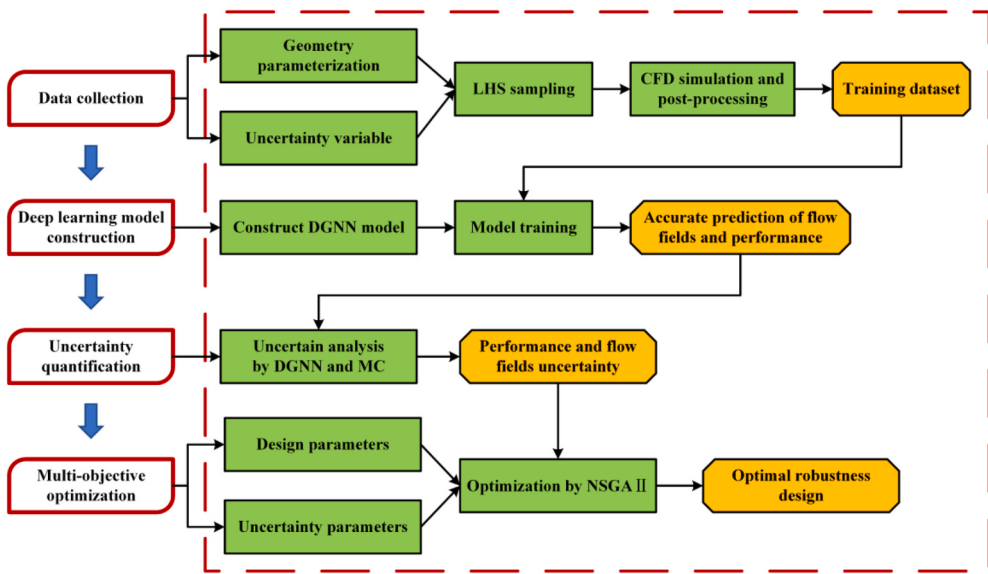


Fig. 1. The overall workflow.

the uncertain response of the turbine performance is solved by combining Monte Carlo (MC) method and the DGNN. In addition, the uncertain response of flow fields, which may be of interest to researchers but is difficult to obtain by conventional surrogate models or numerical simulations, can be obtained by DGNN efficiently. Finally, considering the design variables and uncertainty variables, the multi-objective optimization of the impeller is carried out by the non-dominated ranking genetic algorithm NSGA-II. The optimal solution set with excellent aerodynamic performance and robustness can be achieved.

2.1. CFD analysis

2.1.1. Geometry model

The research object is the impeller of a radial inflow turbine, as shown in Fig. 2, which is designed for a solar-utilizing SCO_2 Brayton cycle. The specifications of the turbine are determined according to the system parameters, and the main geometric parameters are tabulated in Table 1.

2.1.2. CFD method

ANSYS CFX is used to solve the internal flow of the impeller. The flow is assumed to be fully three-dimensional, steady-state, turbulent, compressible, and viscous. The Reynolds time-averaged method combined with the SST turbulence model is used to solve the Navier-Stokes equations. The SST turbulence model combines the near-wall characteristics of the $k-\omega$ model and the insensitivity of the $k-\epsilon$ model to the incoming flow conditions, so it has been widely used in the numerical simulation of turbomachinery. TurboGrid is used for meshing, and a combination of H-O grid topology is used to generate high-quality

Table 1
Main geometric parameters of the impeller.

Parameters	Value
Inlet radius/mm	57.2
Inlet blade height/mm	3.9
Outlet hub radius/mm	16.13
Outlet shroud radius/mm	30.34
Tip clearance/mm	0.2
Blade numbers	15

hexahedral elements. The height of the first layer grid is carefully checked so that y_+ is within the scope recommended by the SST turbulence model. In order to save computational resources and sampling time, CFD analysis is carried out for a single channel. The working medium is SCO_2 . The impeller inlet is given a total temperature of 773 K and a total pressure of 14 MPa. The impeller outlet is given a static pressure of 8 MPa. The rotational speed is 45,000 rpm. The sides of the impeller channel are set as periodically symmetrical surfaces, and all walls are set as adiabatic and smooth walls. In the simulation, the SCO_2 physical properties are obtained by calling real gas property (RGP) tables, where the data are derived from the real CO_2 physical properties in refprop NIST.

Grid independence analysis is performed to ensure the accuracy of simulations. Numerical simulations are carried out with five different grids. The output power and mass flow rate are chosen as criteria, and the results of several candidate grids are calculated as shown in Table 2. The relative error is calculated from the results of the current grid and the upper rough grid. There are no significant changes in the criteria when the grid number exceed 0.2 million. The relative error between the results of 0.2 million grid and 0.3 million grid is 0.31% and 0.33% for mass flow rate and output power. In comprehensive consideration of the

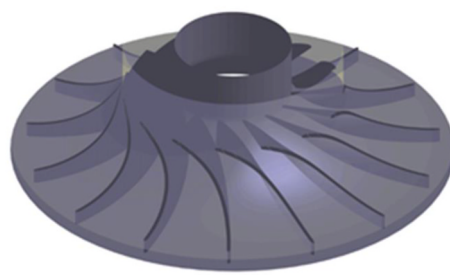


Fig. 2. Turbine impeller.

Table 2
Grid independence analysis.

Group	Element number/ 10^4	Mass flow rate/ $\text{kg} \cdot \text{s}^{-1}$	Relative error/%	Output power/MW	Relative error/%
1	5	6.532	/	467.79	/
2	10	6.741	3.10	486.75	3.90
3	20	6.837	1.40	497.63	2.19
4	30	6.858	0.31	499.28	0.33
5	40	6.858	0.00	499.50	0.04

calculation accuracy and sampling time, the 0.2 million grid is finally used for simulation, and all simulations adopt the same grid configuration. The selected grid is shown in Fig. 3.

2.1.3. Parameterization and dataset collection

The parameterization is valuable and crucial as it determines whether the model can be precisely characterized and determines the parameter space that can be optimized. In this work, the meridional shape, and the angle distribution at various layers are used to parameterize the impeller. Fig. 4 shows the parameterization of the impeller. For the angle distribution, the control sections select the hub section and shroud section, and the angle distribution of other sections is interpolated by the angle distribution of these two sections. Bezier curves with 5 control points are used to represent the hub curve and shroud curve, and Bezier curves with 4 control points are used to represent the hub angle distribution and shroud angle distribution. The general form of Bezier curves can be expressed as:

$$B(t) = \sum_{i=0}^n C_{n,i}(t)x_i, t \in [0, 1] \quad (1)$$

$$C_{n,i}(t) = \frac{n!}{i!(n-i)!}t^i(1-t)^{n-i}$$

Where x_i represents control point i , $B(t)$ corresponds to the curve calculated from the control points.

Since the particular example aims to obtain a robust design without significantly altering the turbine specifications, the first and last control points of the meridional shape are fixed to keep the inlet and outlet blade heights constant. For the convenience of impeller manufacture, the first control point of angle distribution is fixed at 0° . The other control points can be modified and the possible movement direction is shown by arrows in Fig. 4. Therefore, the impeller design parameters consist of 6 meridional shape variables $x_{m1} - x_{m6}$ and 6 angle variables $x_{a1} - x_{a6}$. A total of 5 uncertain parameters are considered in this work, i.e., tip clearance t , inlet total pressure P_{in}^* , inlet total temperature T_{in}^* , outlet static pressure P_{out} , and rotation speed r .

For all variables (12 geometric parameters+5 uncertain parameters), the LHS method is used to generate 5000 sets of samples, and the sample range is shown in Table 3. The flow fields and performance response of 5000 sets of samples are then obtained by CFD calculation and post-processing. The middle span is selected as the target region of flow field prediction. The middle span is widely used in the flow field analysis

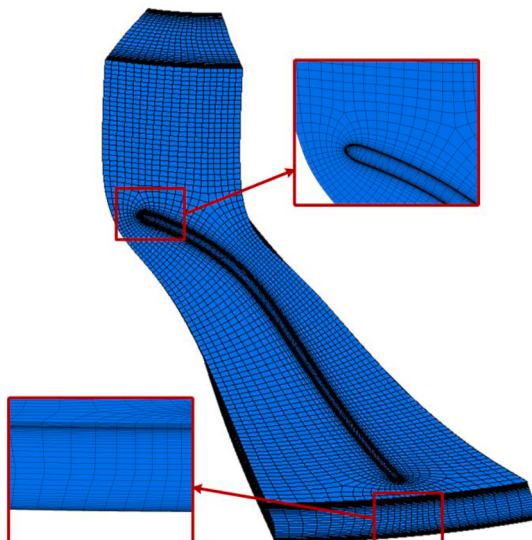


Fig. 3. Grid of single flow channel.

of turbomachinery, which can characterize the internal flow and performance of the turbine to a certain extent. For each sample, the temperature T , pressure P , velocity V , and velocity components of each node on the middle span are output as the true flow fields $\mathbf{f} \in \mathbb{R}^{n \times 6}$. Where n is the number of nodes in the target region. Fig. 5 depicts an example of the extracted flow field. The power, mass flow rate, and total-to-static efficiency are output as the true aerodynamic performance ψ . To deal with the order of magnitude differences between different flow fields and to facilitate network training, all data are normalized to the range of $[-1, 1]$ by the max-min method.

2.2. Graph learning model

The overall network architecture is depicted in Fig. 6. The construction of DGNN is the core of this study. The target is to provide a surrogate model that can quickly predict flow fields and performance, and thus assist the uncertainty quantification of turbomachinery. For this purpose, the DGNN contains two graph learning networks: flow field prediction network and performance discrimination network.

The flow field prediction network maps input variables to flow fields, and the performance discrimination network maps flow fields to aerodynamic performance. The mapping function of two networks can be written as:

$$\begin{cases} \hat{\mathbf{f}} = \hat{F}(\theta, \mathbf{z}, \mathbf{A}; \Theta_F) \\ \hat{\psi} = \hat{Y}(\hat{F}(\theta, \mathbf{z}, \mathbf{A}; \Theta_F), \mathbf{z}, \mathbf{A}; \Theta_Y) \end{cases} \quad (2)$$

Where $\hat{F}(\cdot)$, $\hat{Y}(\cdot)$ denote the mapping functions of flow field prediction network and performance discrimination network, θ represents input feature parameters, \mathbf{z} represents coordinates of grid nodes, \mathbf{A} represents the adjacency matrix, $\hat{\mathbf{f}}$ is the predicted flow fields, $\hat{\psi}$ is the predicted aerodynamic performance, and Θ_F, Θ_Y means the learnable parameters during the training process.

2.2.1. Network configuration

To use graph learning methods for field prediction, the pre-processing and precise representation of fields are crucial. Traditional CNNs based deep learning methods need structured field data. Most scholars address this problem by dividing the structured mesh in the meshing stage or pixelating the fields. The limitations of these methods are obvious and fatal. Structured mesh requires extra tedious work, and unstructured mesh is unavoidable for complex geometry. Pixelation will result in local information loss, especially for fields where exist drastic geometry changes or large physical field gradients. Therefore, we innovatively use graph data to describe the flow fields on grids and construct the network architecture under the frame of GNNs.

The concerned flow field region is mathematically expressed as a graph $G = \{V, E\}$, where V is the set of nodes and E represents the grid connection relations. In addition, the adjacency matrix A describes the adjacency relationships between nodes and $A_{ij} = 1$ if $e_{ij} \in E$. Feature matrix $\mathbf{X} \in \mathbb{R}^{n \times d}$ is used to represent the predefined field attributes at each grid. This approach not only ensures the high accuracy of flow field data but also preserves many excellent properties of grids, such as the non-uniformity of the grid spacing.

The specific architecture of our model is shown in Fig. 7. The upper part is the flow field prediction network, and the lower part is the performance discrimination network. The input feature parameters of the flow field prediction network are geometric parameters, uncertain parameters, and spatial coordinates of nodes in three directions. The concerned flow field region is the middle span of the impeller. Firstly, the features of input parameters are extracted by 4 feature extraction blocks. The feature extraction block is a combination of a graph convolutional layer and an activation function. Then, the extracted features are mapped to the target flow fields at grid vertices by a graph convolutional layer. For the performance discrimination network, the target

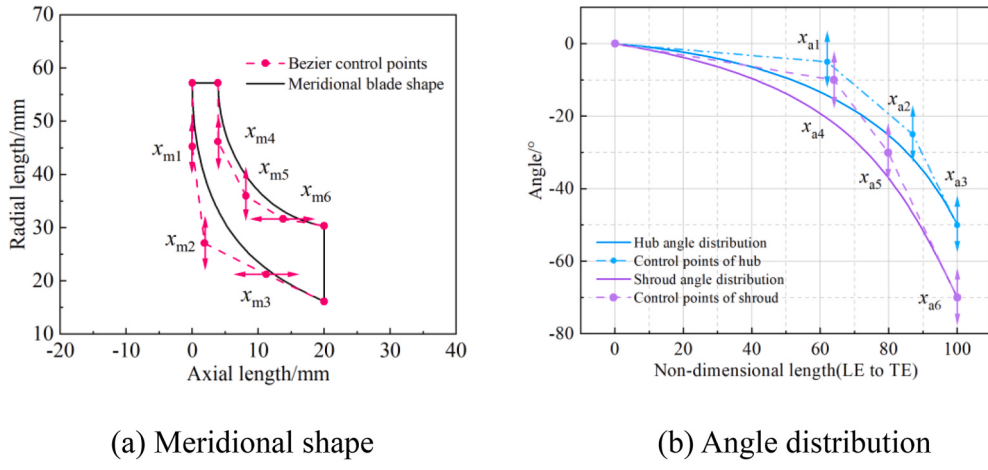


Fig. 4. Parameterization of the impeller.

Table 3

Detail of geometric and uncertain parameters.

Angle	x_{a1}	x_{a2}	x_{a3}	x_{a4}	x_{a5}	x_{a6}
Range	[-15, -2.5]	[-35, -15]	[-60, -40]	[5, 20]	[20, 40]	[60, 80]
Meridional	x_{m1}	x_{m2}	x_{m3}	x_{m4}	x_{m5}	x_{m6}
Range	[40.74, 49.78]	[24.4, 29.8]	[10, 12.3]	[41.58, 50.82]	[32.4, 39.6]	[12.4, 15.16]
Uncertain	t	P_{in}^*	T_{in}^*	P_{out}	r	Uncertain
Range	[0.15, 0.25]	[13.72, 14.28]	[763, 783]	[7.644, 7.956]	[44,000, 46,000]	Range

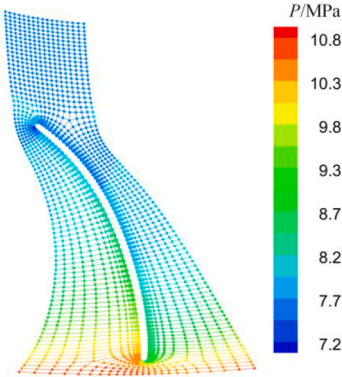


Fig. 5. Example of the extracted flow field.

flow fields at grid vertices and spatial coordinates of nodes are spliced as the input. 4 down-sampling blocks are used to extract flow field features layer by layer. Down-sampling block 1 contains a graph convolutional layer, an activation function, a graph pooling layer, and a readout layer. The graph pooling layer is used to filter nodes and retain useful nodes for the next layer, and the readout layer reads out the representation of the whole graph. Down-sampling block 2 has no readout layer, and its output is extracted by a readout layer. Then, the readout results of each layer are added together, and the predicted turbine performance is output through several FC (fully connected) layers. It is worth highlighting that the DGNN has no restrictions on the flow field region and grid form, and users can conveniently extend this method to arbitrary 3D flow field prediction tasks.

As the core part of the DGNN model, graph convolutional operations act directly on graph data and are a current research hotspot [47]. It can handle non-Euclidean data that cannot be handled by traditional CNNs. For GNNs, the feature vectors of a node in layer $l+1$ are computed through the feature vectors of the node and its neighbor nodes on the previous layer. Consequently, a node adjacency matrix is indispensable

in GNNs to ensure that node adjacencies are fully characterized. The generalized form of GNNs is:

$$\mathbf{X}^{l+1} = f(\mathbf{X}^l, \mathbf{A}) \quad (3)$$

Where $f(\cdot)$ denotes an activation function.

The detailed network structure is shown in Table 4. The graph convolutional operation in this work adopts GraphSAGE [48]. Its main purpose is to learn a node representation method, i.e., how to sample and aggregate node features from its partial neighbors, instead of training a separate aggregation mapping (embedding) for each node. It randomly samples a fixed number of neighbor nodes instead of considering all neighbors. Its graph convolution operation is defined as:

$$\mathbf{x}_i^{l+1} = f\left(\mathbf{W}_1 \cdot f_a\left(\mathbf{x}_i^l, \left\{\mathbf{x}_j^l, \forall j \in \mathcal{N}(i)\right\}\right)\right) \quad (4)$$

Where $f_a(\cdot)$ is an aggregation function, $\mathcal{N}(i)$ donates the neighbor nodes of node i .

GELU [49] is adopted for the activation function. It is essentially a combination of Dropout (randomly deactivating some neurons during training) and ReLU. It is a novel activation function that can effectively suppress overfitting and enhance the generalization performance of the model. In the actual calculation, GELU can be approximately expressed as :

$$\text{GELU}(x) = 0.5x \cdot \left[1 + \tanh\left[\sqrt{2/\pi} (x + 0.44715x^2)\right]\right] \quad (5)$$

In addition, topkpooling [50] is used for graph pooling. It calculates projection scores for each node with the help of a projection vector and selects top-k nodes according to the scores.

MSEloss [51] is adopted for both sub-networks, and it can be expressed as:

$$\mathcal{L}_F = \mathcal{L}(\mathbf{f}, \hat{\mathbf{f}}) = \mathcal{L}(\|\mathbf{f} - \hat{\mathbf{f}}(\mathbf{\theta}, \mathbf{z}, \mathbf{A}; \Theta_F)\|) \quad (6)$$

$$\mathcal{L}_Y = \mathcal{L}(\Psi, \hat{\Psi}) = \mathcal{L}(\|\Psi - \hat{\Psi}(\mathbf{\theta}, \mathbf{z}, \mathbf{A}; \Theta_F), \mathbf{z}, \mathbf{A}; \Theta_Y\|) \quad (7)$$

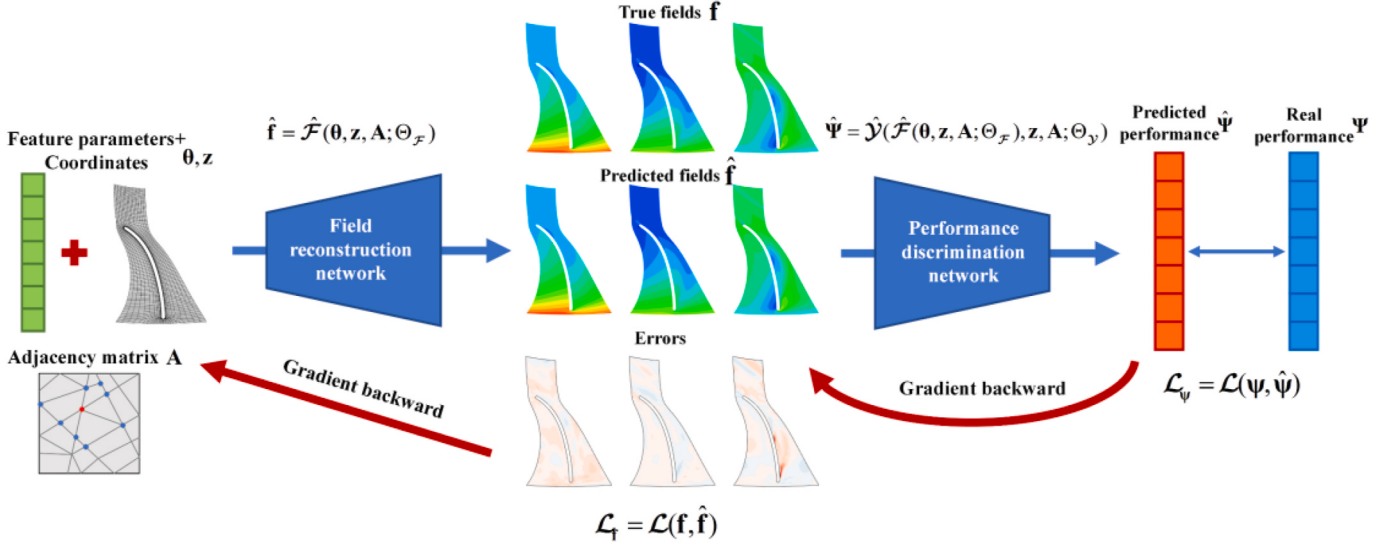


Fig. 6. The architecture of DGNN.

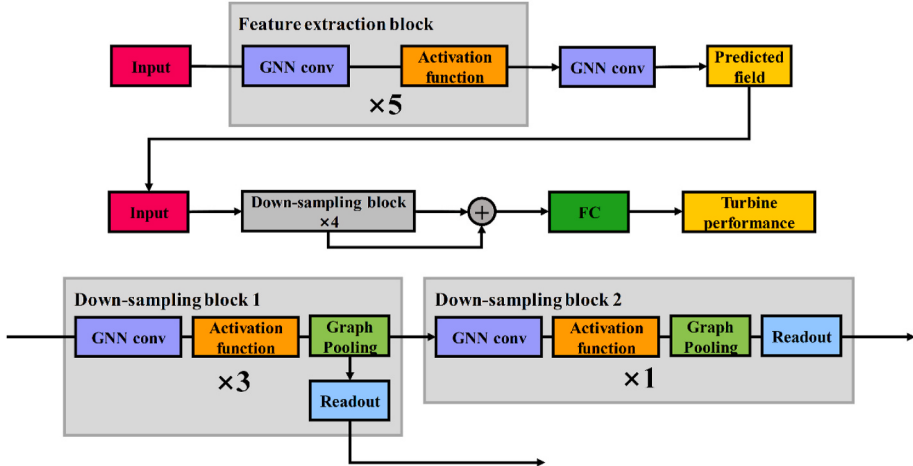


Fig. 7. The specific architecture of the DGNN.

Where $\mathcal{L}(\cdot)$ denotes the loss function.

2.2.2. Training strategy

The database constructed in the previous step is used to train the network. The raw dataset is divided into the training set, validation set, and test set according to the proportion of 70%, 10%, and 20%. Two sub-networks can be trained simultaneously or separately. The training process is the optimization of the learnable parameters to minimize loss functions, and it can be written in the following form:

$$\Theta_F = \underset{\Theta_F}{\operatorname{argmin}} \left\{ \mathbb{E}_{\{\theta, z, A, f\} \sim \mathcal{D}} (\mathcal{L}_F) \right\} \quad (8)$$

$$\Theta_Y = \underset{\Theta_Y}{\operatorname{argmin}} \left\{ \mathbb{E}_{\{f, z, A, \Psi\} \sim \mathcal{D}} (\mathcal{L}_{\Psi}) \right\} \quad (9)$$

Where $\{\theta, z, A, f\} \sim \mathcal{D}$ and $\{f, z, A, \Psi\} \sim \mathcal{D}$ respectively represents the training dataset of the flow field prediction network and the performance discrimination network.

In the training process, the performance discrimination network is successively trained with real flow fields and predicted flow fields to accelerate the convergence. Specifically, the performance discrimination network is trained with real flow fields in the first 200 epochs, after which the results of the flow field prediction network are used. The

selected network optimizer is ADAM [52]. The initial learning rates of the flow field prediction network and the performance discrimination network are 0.005 and 0.002, respectively. The learning rates decrease to 0.1 of the original value when the epoch reaches 200, 300, and 400.

2.3. Model accuracy criteria and uncertainty quantification metrics

To evaluate the accuracy of the flow field prediction network, field mean squared error (FMSE) is adopted and computed for each sample, and the equation is as follows:

$$\text{FMSE} = \frac{1}{n} \sum_{j=1}^n (\mathbf{f}^{j,m} - \hat{\mathbf{f}}^{j,m})^2 \quad (10)$$

Where m represents the m -th flow field characteristic, j represents j -th node in a graph.

Target relative error (TRE) is used for the performance discrimination network, and its definition is:

$$\text{TRE} = \frac{\Psi^s - \hat{\Psi}^s}{\Psi^s} \quad (11)$$

Where s represents the s -th turbine performance parameters.

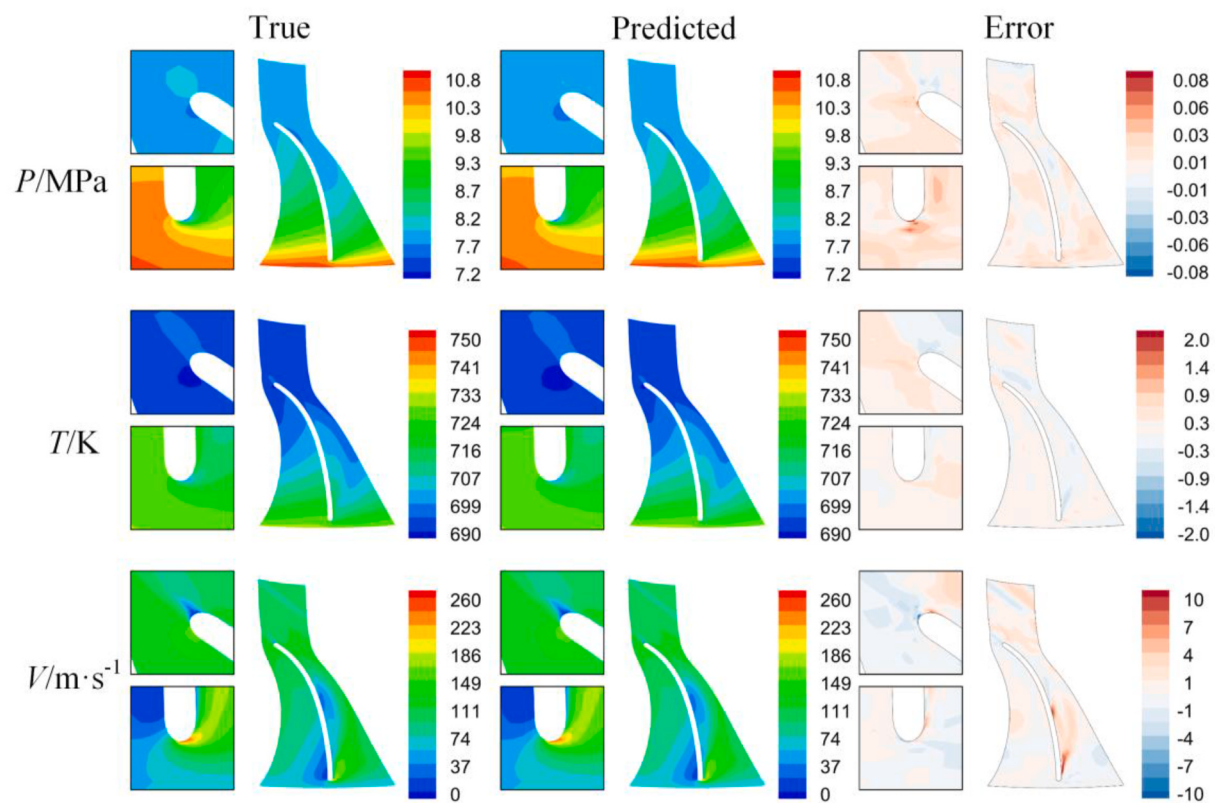


Fig. 8. Flow fields comparison of test set samples (case A).

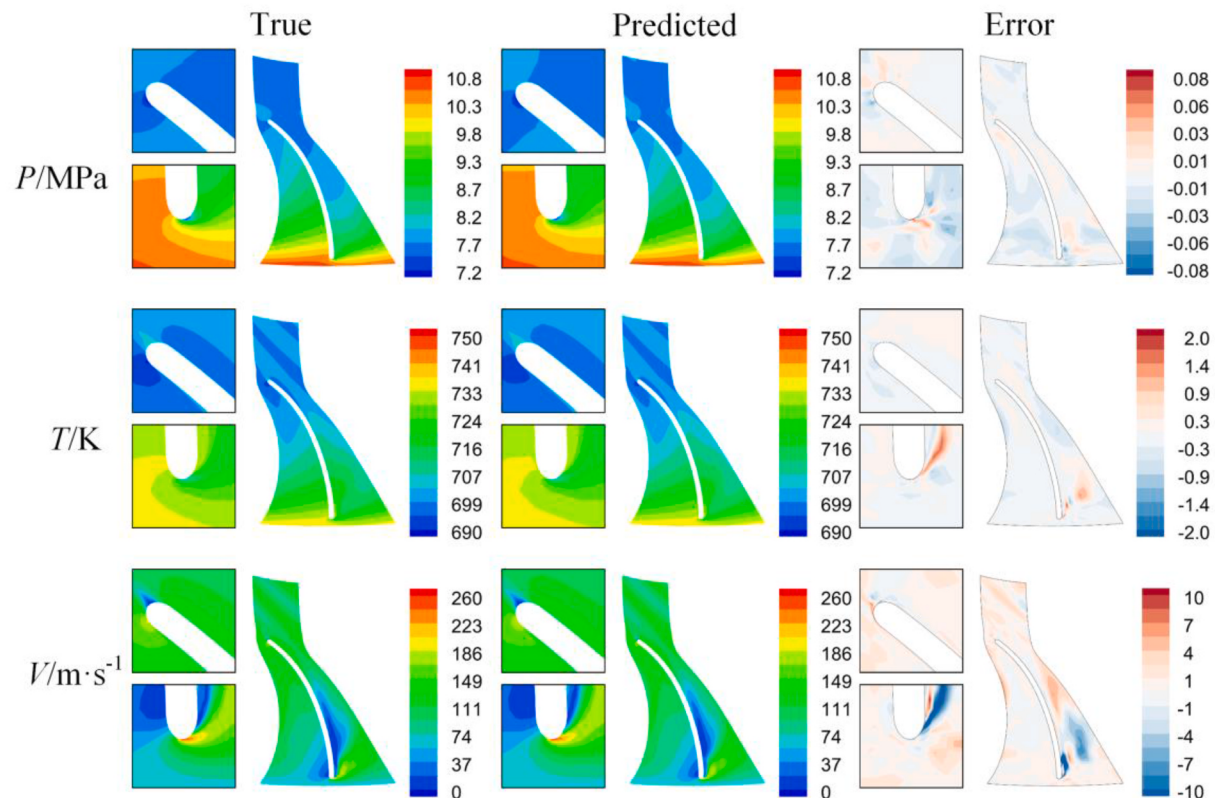


Fig. 9. Flow fields comparison of test set samples (case B).

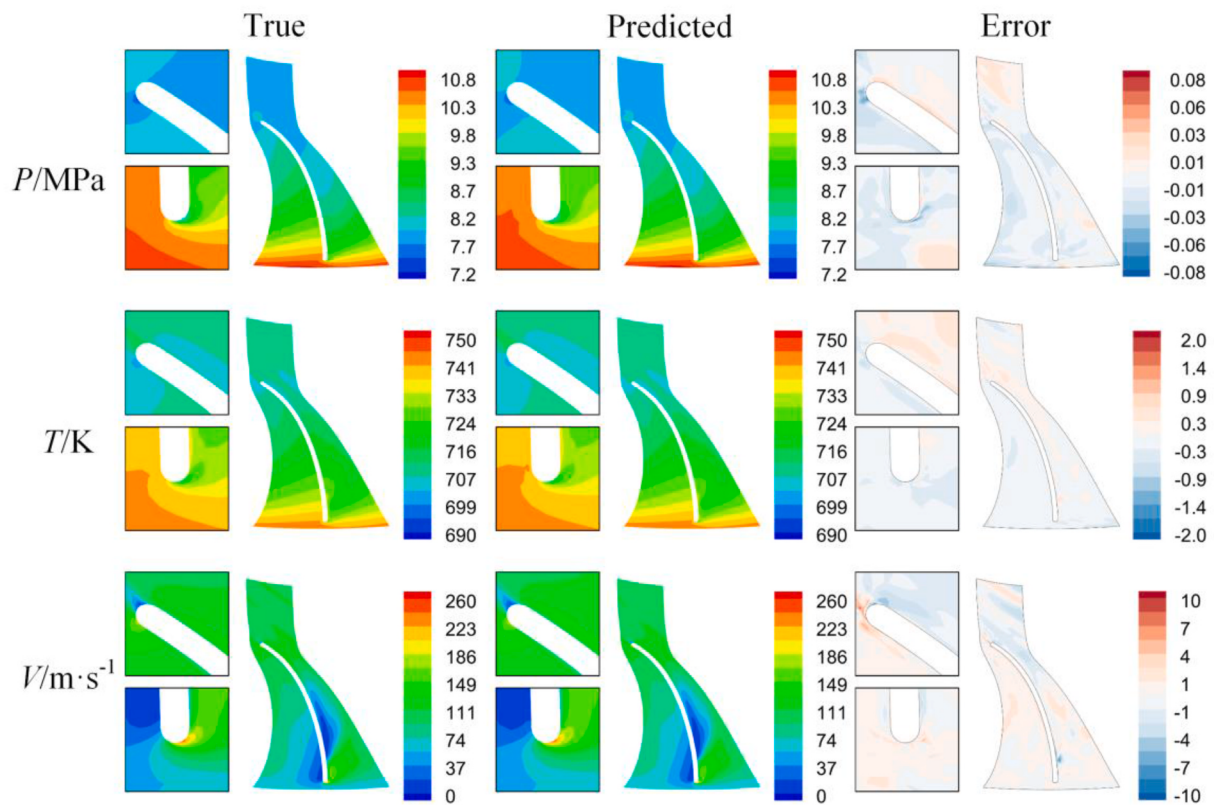


Fig. 10. Flow fields comparison of the test set samples (case C).

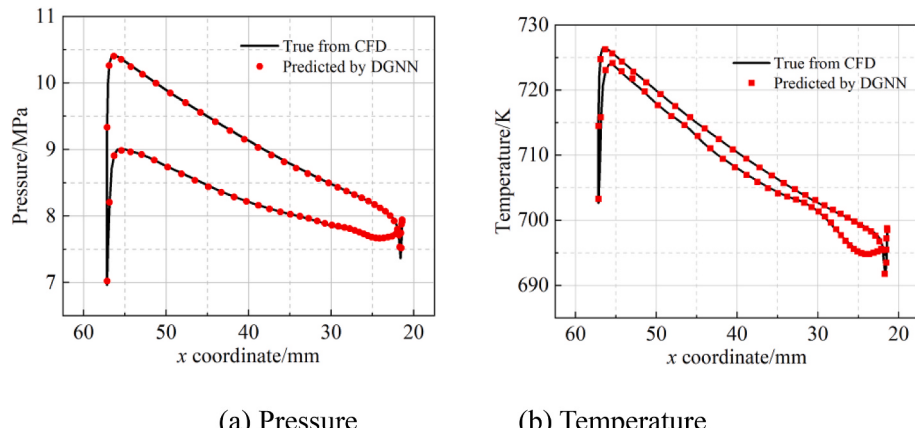


Fig. 11. Flow field distributions on the blade surface (case A).

In addition, mean absolute error (MAE) and root mean squared error (RMSE) are used to evaluate the overall performance of the performance discrimination network and calculated by:

$$\text{MAE} = \frac{1}{N} \sum_{i=1}^N |\hat{\Psi}^{i,s} - \Psi^{i,s}| \quad (12)$$

$$\text{RMSE} = \sqrt{\frac{1}{N} \sum_{i=1}^N (\hat{\Psi}^{i,s} - \Psi^{i,s})^2} \quad (13)$$

Where N is the number of samples.

After the construction of the high-precision DGNN, the uncertain response of fields and performance can be obtained by combining the MC method and the DGNN. In this work, the uncertainty of turbine

performance is quantified by standard deviation. The sensitivity of flow fields is quantified by the field point-wise coefficient of variation (FPCV) is adopted:

$$\text{FPCV} = \frac{\sigma_{\Psi^{i,m}}}{\bar{\Psi}^{i,m}} \quad (14)$$

FPCV denotes the ratio of standard deviation σ to mean value and a larger FPCV means a larger sensitivity.

2.4. Multi-objective robust optimization

Thanks to the advantages of fast speed, low computational complexity, and good convergence, NSGA-II is widely used in the multi-objective optimization of turbomachinery. In this work, the optimization code is provided by the Geatpy package in Python. The population

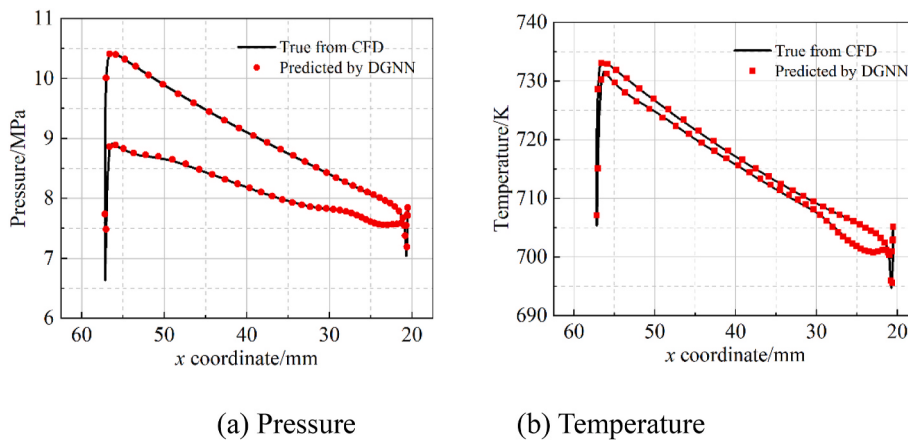


Fig. 12. Flow field distribution on the blade surface (case B).

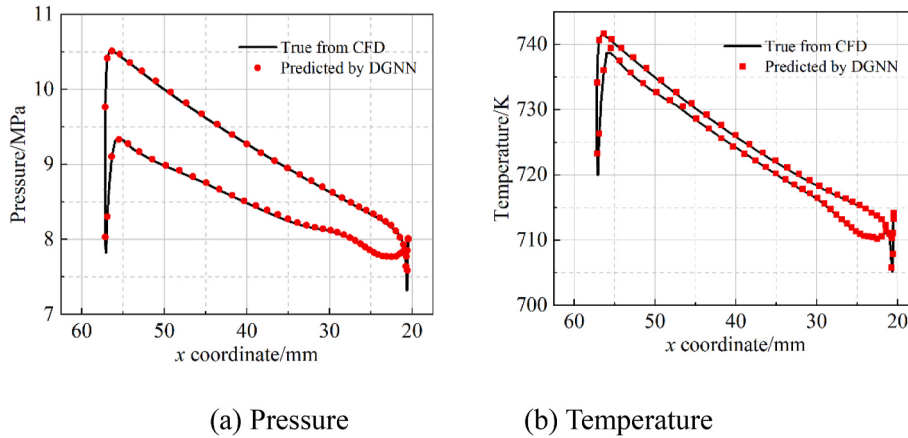


Fig. 13. Flow field distribution on the blade surface (case C).

Table 4

The detailed network structure.

Flow field prediction network			Performance discrimination Network		
Name	Layer type	Output size	Name	Layer type	Output size
Input		$n \times 20$	Input		$n \times 9$
Feature extract block	SAGEconv +GELU	$n \times 64$	Down-sampling block 1	SAGEconv +GELU + topkpooling +readput	$0.8n \times 64$
Feature extract block	SAGEconv +GELU	$n \times 128$	Down-sampling block 1	SAGEconv +GELU + topkpooling +readput	$0.64n \times 64$
Feature extract block	SAGEconv +GELU	$n \times 128$	Down-sampling block 1	SAGEconv +GELU + topkpooling +readput	$0.512n \times 64$
Feature extract block	SAGEconv +GELU	$n \times 128$	Down-sampling block 2	SAGEconv +GELU + topkpooling +readput	128
Feature extract block	SAGEconv +GELU	$n \times 64$	readout module	global max pooling+ global mean pooling	128
Graph convolutional layer	SAGEconv	$n \times 6$	FC	fully connected+ fully connected+ fully connected	64 64 3

size is 200, the maximum number of generations is 100, the crossover probability is set as 0.9, and the mutation probability is set as 0.1. The optimization variables are geometric parameters x_{a1} - x_{a6} and x_{m1} - x_{m6} , and the uncertainties are tip clearance t , inlet total pressure P_{in}^* , inlet total temperature T_{in}^* , outlet static pressure P_{out} , and rotation speed r . The boundaries of geometric parameters and uncertainties are the same

as the sampling range listed in Table 3. The power and efficiency of the turbine directly affect the work capacity and economy of the energy system, so robust optimization is performed for power and efficiency, respectively. The mathematical representation of the optimization is:

$$\begin{cases} \operatorname{argmax}(\bar{W}), \operatorname{argmin}(\sigma_w) \\ x = (x_{a1} - x_{a6}, x_{m1} - x_{m6}) \\ u = (t, P_{in}^*, T_{in}^*, P_{out}) \end{cases} \quad (15)$$

$$\begin{cases} \operatorname{argmax}(\bar{\eta}), \operatorname{argmin}(\sigma_\eta) \\ x = (x_{a1} - x_{a6}, x_{m1} - x_{m6}) \\ u = (t, P_{in}^*, T_{in}^*, P_{out}) \end{cases} \quad (16)$$

3. Results and discussion

In this section, the superiority of the proposed graph learning method is illustrated by prediction accuracy and time consumption firstly. Then, uncertainty responses of the flow fields and turbine performance are obtained by the DGNN and MC method. Finally, robust optimizations are carried out for power and efficiency.

3.1. The performance of DGNN

3.1.1. Flow fields reconstruction

In this research, the proposed DGNN is implemented through PyTorch Geometric [53] and trained by NVIDIA GTX1080Ti for 500 epochs with a batch size of 32. Figs. 8–10 shows the comparison of the predicted flow fields and the real flow field for three random samples in the test set. As can be seen from the true flow fields, the turbine pressure and temperature gradually decrease from inlet to outlet; the pressure on the pressure side is greater than that on the suction side; the positive attack angle results in a low-velocity region on the pressure side of the leading edge; a local low-speed region exists on the suction side due to the coupling effect of the positive attack angle and the leakage flow. The predicted flow fields are in good agreement with the real flow fields, and the DGNN can reconstruct the above flow phenomenon with a small error. It is worth pointing out that the corresponding error increases in the complex flow region, but it is completely within acceptable ranges.

The flow field distributions on the blade surface directly affect the work capacity and safety of turbomachinery. As depicted in Figs. 11–13, the predicted distribution matches the actual distribution remarkably well. The complex flow field distribution at the leading and trailing edges is well captured.

To further quantify the flow field prediction performance, the FMSE is calculated for the test set samples, as presented in Fig. 14. High prediction accuracy is obtained, and the FMSE of all fields is less than 5×10^{-4} for most samples. It once again demonstrates the high reliability of DGNN for flow field prediction.

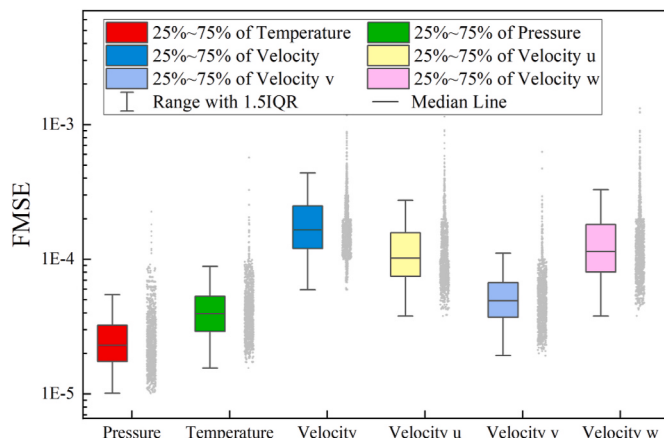


Fig. 14. Prediction errors of flow field prediction network.

3.1.2. Aerodynamic performance prediction

Fig. 15 shows the error distributions of predicted turbine performance. It can be observed that the mass flow rate ranges from 6.43 kg s^{-1} to 7.17 kg s^{-1} , the power ranges from 449 kW to 563 kW, and the efficiency range from 0.87 to 0.93. The prediction accuracy of efficiency is the highest, followed by the mass flow rate, and the prediction accuracy of power is inferior. Overall, for all performance metrics, most of the samples fall near the $y = x$ line and are within the 1% error band.

To further validate the accuracy of our model, several classical surrogate models are constructed and compared with the DGNN model. The classical surrogate models choose Polynomial Regression (PR), Random Forest (RF), Supported Vector Regression (SVR), and Gaussian Process Regression (GPR). For these models, the input parameters are directly used to predict the aerodynamic performance parameters, and the flow fields are ignored. All these surrogate models are implemented through a machine learning library in Python named Sklearn [54]. After tedious coarse and fine tuning, the optimal hyper-parameters for each model are summarized in Table 5.

As can be seen from the box plot in Fig. 16, the DGNN model has a lower value of TRE for all aerodynamic performance parameters. 25%–75% of TRE for all performance metrics is less than 0.5%. The error statistics of different models from Table 6 further clarify the superiority of the DGNN. DGNN shows better accuracy (minimum MAE and RMSE) for all performance parameters. The performance parameter is generally an abstract extraction of flow fields. DGNN can not only provide precise flow fields but also accurately identify the aerodynamic performance based on flow fields instead of simply input parameters. Compared to classical surrogate models that directly map design parameters to performance parameters, the proposed model is helpful for researchers to further understand the relationship between performance and flow fields.

3.1.3. Effect of training size

In this instance, 5000 sets of samples are generated and DGNN achieves excellent performance with a training size of 0.7. However, such a quantity of high-fidelity data may be unavailable in practice. Therefore, determining the minimum training data required for high-accuracy deep learning models has been a hot research topic.

Fig. 17 shows the impact of training set size on network performance. An obvious observation is that the error of both sub-networks decreases as the training set increases. With a training size of 0.1, 75% of FMSE for temperature and pressure fields is less than 1.5×10^{-4} and 75% of FMSE for velocity fields is less than 7×10^{-4} . The 1.5 interquartile range of TRE for all performance metrics is within $\pm 2\%$ when the training size is 0.1. The results of FMSE and TRE indicate that DGNN with a training size of 0.3 can achieve satisfactory performance. Increasing the training size from 0.3 to 0.7 will further improve the prediction performance, but the improvement is limited. It can be concluded that the performance of DGNN benefits from the number of training samples. In addition, the proposed model can also provide satisfactory results with small training samples.

3.1.4. Comparison of computation cost

The computation costs of CFD and the proposed DGNN are compared in Table 7. The CFD calculations are conducted on Intel Xeon W2265 processors with 16 cores. The training and evaluation of DGNN are completed by NVIDIA Geforce-1080Ti. The graph learning method performs parallel operations on tensors, which means that it can predict multiple cases simultaneously through a batch operation and apportion the calculation cost of each sample. In this example, the batch size is 32 for network training and evaluation. The graph learning networks on GPU can predict the turbine performance along with flow fields within 0.02s, which is 4 orders faster than CFD solvers. The evaluation time of the DGNN can be further reduced as the batch size increases. It is admittedly true that DGNN requires a lot of sampling time and training time, but once the network training is completed, it shows considerable

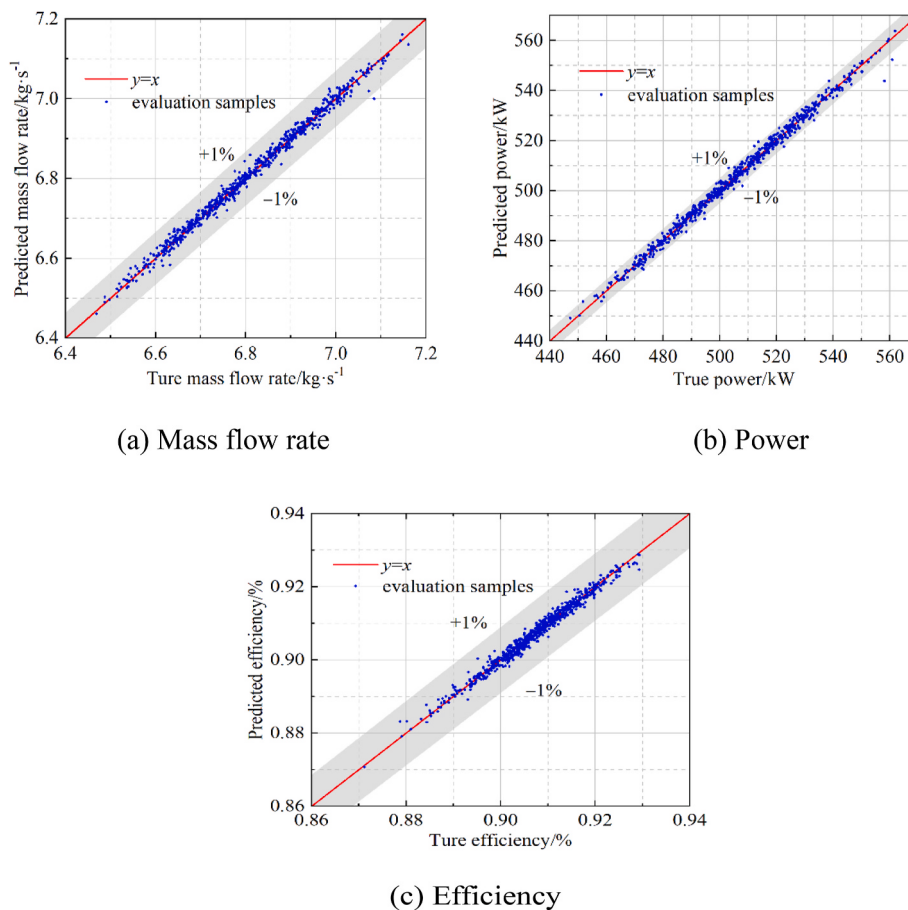


Fig. 15. Scatter plot of the predicted aerodynamic performance.

Table 5
Classical surrogate models configuration.

classical surrogate models	Hyper-parameter
PR	polynomial features = 3
RF	max depth = 20; n estimators = 100; criterion = 'mse'; oob score = False; max features = 'auto'
SVR	degree = 3; kernel = 'rbf'; C = 10; gamma = 0.13; epsilon = 0.01
GPR	kernel: 'RBF'; n_restarts_optimizer = 2; optimizer = fmin_l_bfgs_b; normalize_y = True

Table 6
The error statistics of different models.

	Mass flow		Power		Efficiency	
	MAE	RMSE	MAE	RMSE	MAE	RMSE
PR	0.0193	0.0251	3.0510	3.9493	0.0023	0.0029
RF	0.0253	0.0327	4.1811	5.2881	0.0032	0.0042
SVR	0.0178	0.0237	2.7837	3.7391	0.0016	0.0022
GPR	0.0156	0.0203	2.2454	2.9414	0.0018	0.0025
DGNN	0.0106	0.0142	1.4237	1.9462	0.0010	0.0014

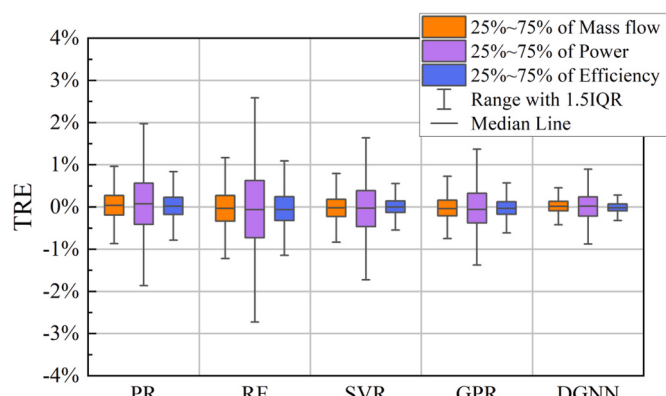


Fig. 16 Box plot of the prediction errors for different models

potential as an alternative to CFD solvers. Based on the great regression accuracy and near the real-time speed of the DGNN model, uncertainty quantification and multi-objective optimization are further performed for the impeller.

3.2. Uncertainty quantification

The effects of coupled uncertainties on the turbine performance and flow field are analyzed by combining the DGNN and Monte Carlo method. Geometric uncertainty selects tip clearance, and thermodynamic uncertainties choose inlet total pressure, inlet total temperature, and outlet static pressure. Rotation speed uncertainty is also considered. Assume that all uncertainties satisfy normal distribution, and the detailed boundary can be found in [Table 3](#). A total of 5000 MC samples are calculated.

Fig. 18 shows the effects of geometric errors, fluctuations of thermodynamic parameters, speed fluctuations, and coupling effects on the turbine performance. Geometric uncertainty has the least effect on power, followed by rotation speed uncertainty, while thermodynamic

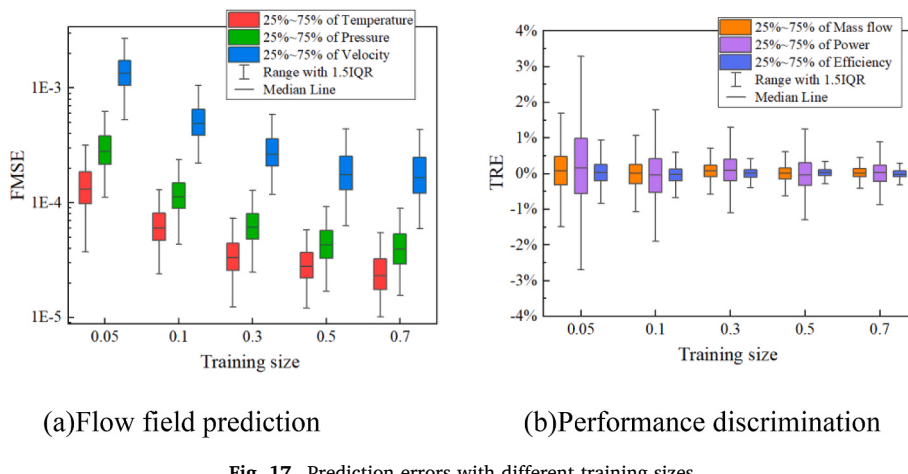


Fig. 17. Prediction errors with different training sizes.

Table 7
Computation costs comparison.

method	Memory cost/Mb	Model size/Mb	Sampling time/h	Training time/h	evaluation time/s
CFD	1550	/	/	/	270
DGNN	2150	0.55	375	4	0.02

uncertainties dominate the variation of turbine power. For turbine efficiency, the impact of geometric uncertainty and thermodynamic uncertainties are similar and slightly larger than that of rotation speed uncertainty. The coupling effects are not a straightforward superposition of single effects. Considering the coupling effect of all uncertainties, the mean power is 494.93 kW and the standard deviation is 9.32, while the mean value of the efficiency is 90.42% and the standard deviation is 2.58×10^{-3} . The fluctuation range of power is much larger, the maximum deviation of the power is 6.74% of the statistical values, and the maximum deviation of efficiency is 1.07%.

A remarkable advantage of the proposed model is that the turbine performance and flow fields can be obtained in almost real-time. This makes it dominant over the traditional surrogate models and CFD analysis. The former completely ignores the flow field data, while the latter requires a lot of computational resources and time. Thanks to the speed of DGNN, researchers can conveniently obtain the uncertain response of whole flow fields. It is beneficial to further reveal the flow mechanism under the influence of uncertainties.

Nominal flow fields, the statistical mean value of flow fields under input uncertainties, and the uncertain response of flow fields are

depicted in Fig. 19. The statistical mean value of the flow fields is similar to the nominal case. From the FPCV distribution, it can be seen that the maximum fluctuations of all fields occur near the blade surface region, especially near the leading edge. The uncertain response varies for different flow fields. The velocity field is more sensitive to input uncertainties, and the region with the maximum value of FPCV is located on the suction side of the blade near the leading edge. To intuitively show the flow field sensitivity, the mean, maximum, and minimum values of FPCV are tabulated in Table 8. The smallest mean FPCV corresponds to the temperature field. The maximum FPCV belongs to the velocity field with a value of 0.3451. It can be explained that the velocity field is more complex than the pressure and temperature fields. The changes in tip clearance, the fluctuations of thermodynamic parameters, and the fluctuations of rotation speed can lead to large variations in the velocity field, especially in areas with poor flow conditions.

The flow fields and standard deviation distributions on the blade surface are derived as presented in Fig. 20. The region between the red line and the cyan line represents the field uncertainty. The temperature fluctuation on the blade surface is small, indicating that the temperature field is less sensitive to input uncertainties. It is consistent with the conclusion of the whole field analysis mentioned above. For the pressure field, the fluctuation at the suction surface is more extensive than at the pressure surface. The pressure uncertainty is almost constant along the flow direction except for the leading edge. The most sensitive region is located at the suction side of the leading edge, where flow acceleration exists.

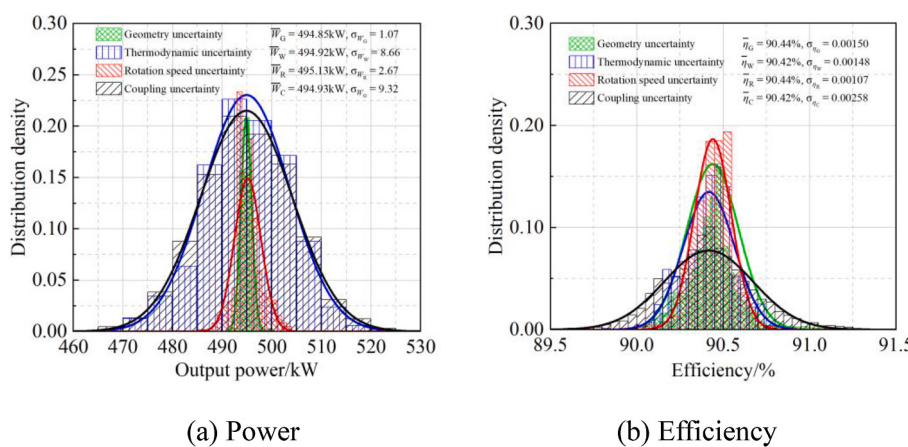


Fig. 18. Uncertain response of turbine performance.

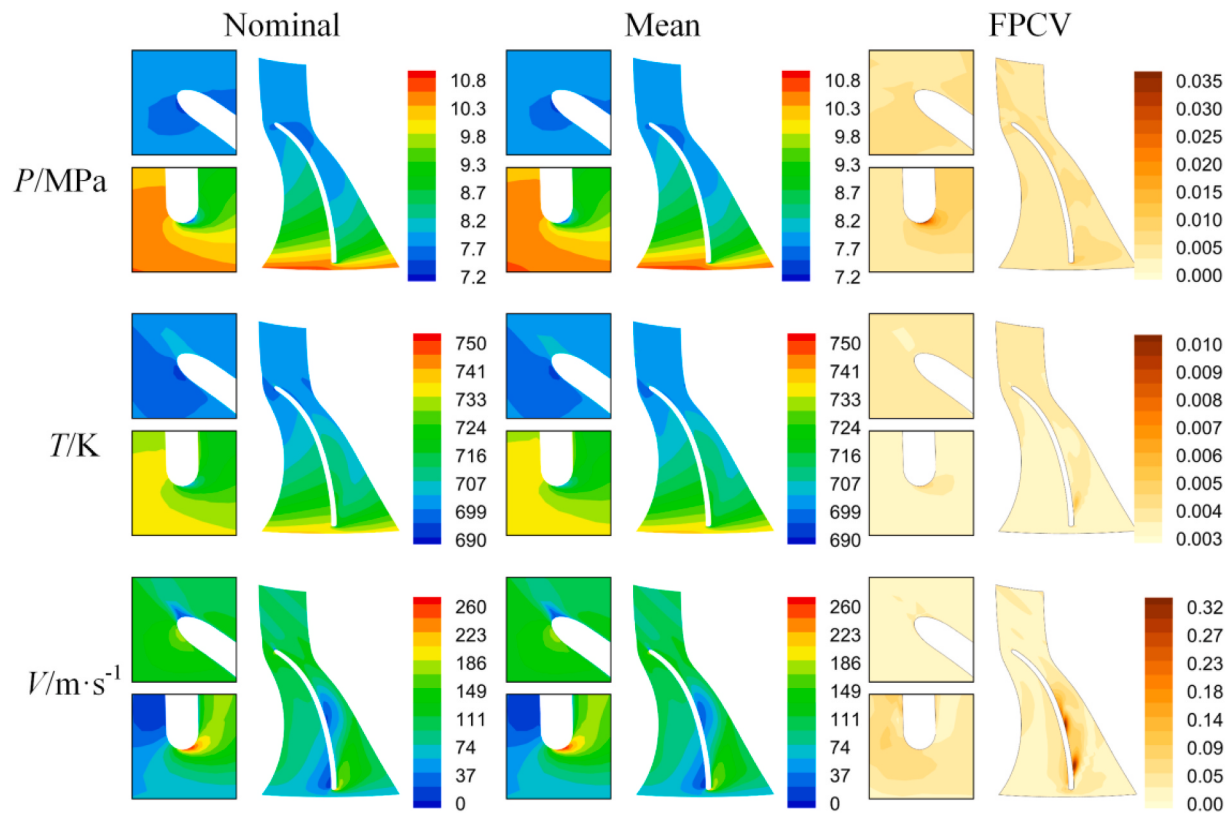


Fig. 19. Nominal flow fields, the statistical mean value of flow fields, and the FPCV of flow fields.

Table 8
Fields uncertainty quantification through FPCV.

FPCV	Pressure	Temperature	Velocity
Mean	0.0052	0.0036	0.0479
Maximum	0.0371	0.0056	0.3451

3.3. Multi-objective robust optimization

According to the optimization strategy, the multi-objective optimizations of the impeller are performed for two optimization objectives (power robustness and efficiency robustness). The obtained Pareto front solutions for two optimization objectives are presented in Fig. 21. For the Pareto frontier of power robust optimization in Fig. 21 (a), the maximum power increases by 3.94%, while the standard deviation

increases by 0.32%. The minimum standard deviation decreases by 27.58%, while the power decreases by 2.73%. As for the results of the efficiency robust optimization, the standard deviations of all Pareto solutions are lower than that of the initial impeller. The maximum efficiency case improves the efficiency by 1.88% (absolute value) and reduces the standard deviation by 21.47%. The minimum standard deviation case reduces the standard deviation by 64.03% and slightly decreases the efficiency by 0.52% (absolute value).

The improvement of mean efficiency and mean power is relatively limited. On the one hand, the optimization space is limited considering the stability of the structure. On the other hand, it reveals that the original impeller is well-designed. The robustness is significantly improved, especially for efficiency. This proves the effectiveness of our method. It also indicates that performance uncertainties are often neglected in the general design optimization process, and thus robust

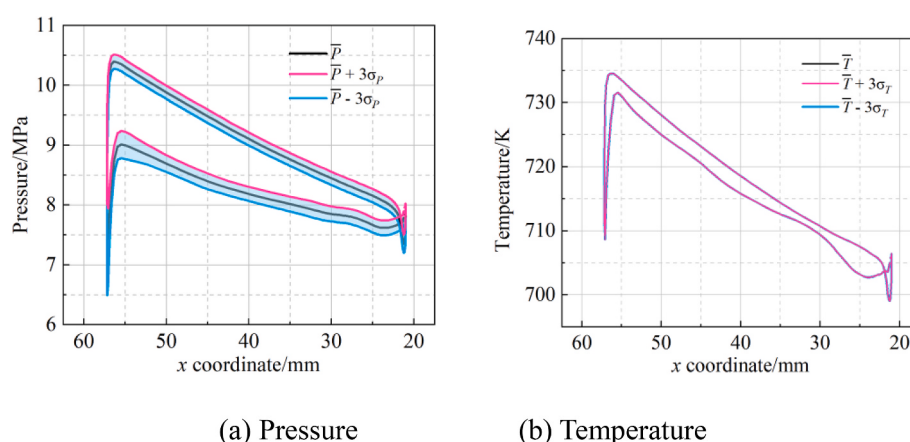


Fig. 20. Flow fields and uncertainty distributions on the blade surface.

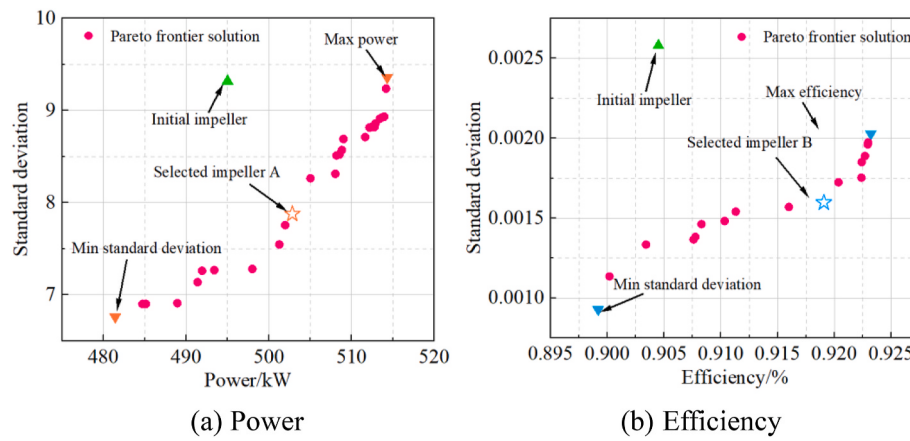


Fig. 21. Pareto frontier of robust optimization.

optimization is necessary. Two optimized impellers are selected and marked as A and B for further comparison, as depicted by the star shape in Fig. 21.

The geometry comparison of the initial impeller, impeller A, and

impeller B is presented in Fig. 22. For a clearer view of the geometric difference, one blade of impeller A and impeller B is hidden in Fig. 22 (c). Impeller A and impeller B tend to have a narrower meridional shape in the middle of the flow channel. Impeller A has a bigger hub-to-shroud

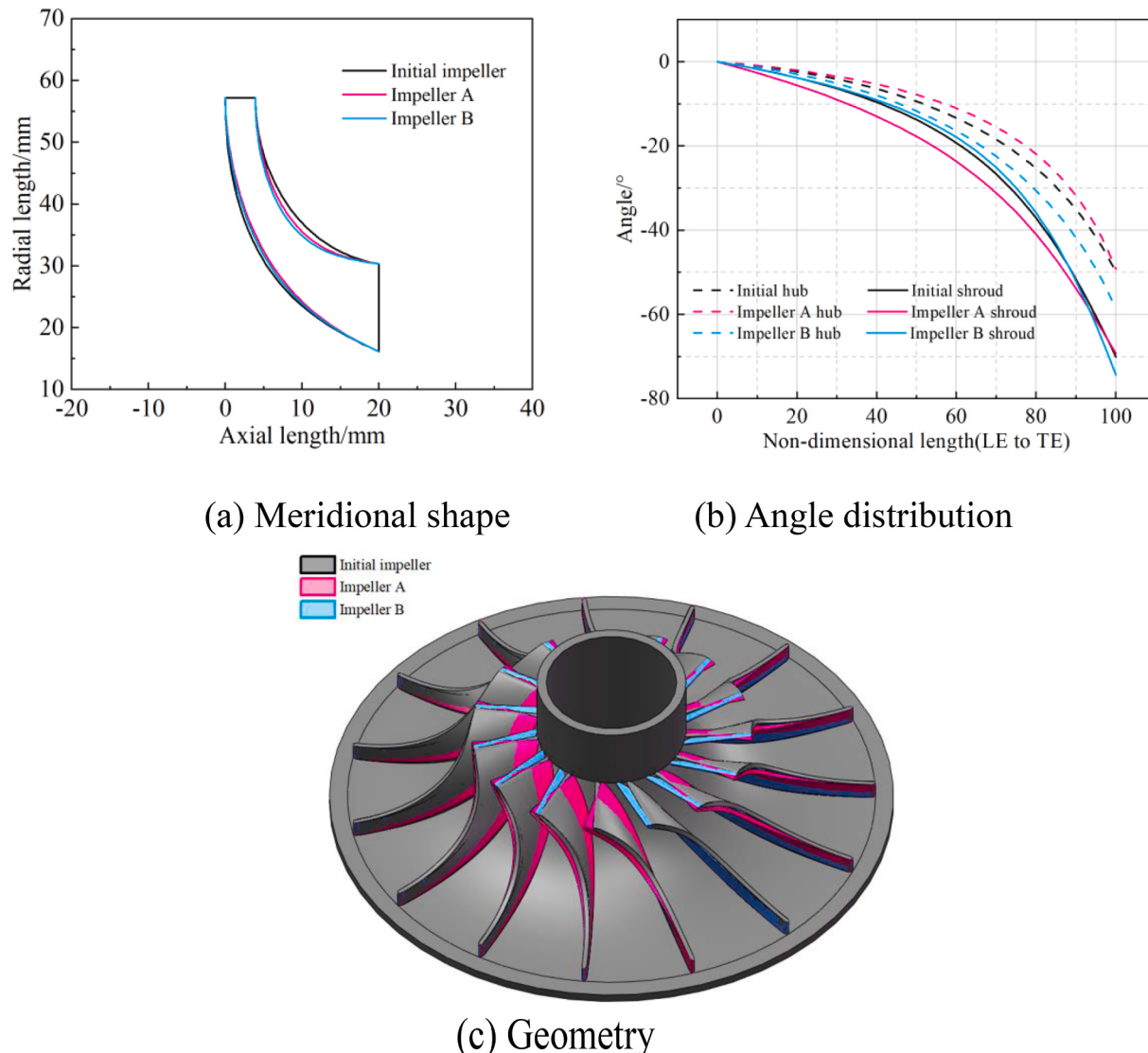


Fig. 22. Geometry comparison.

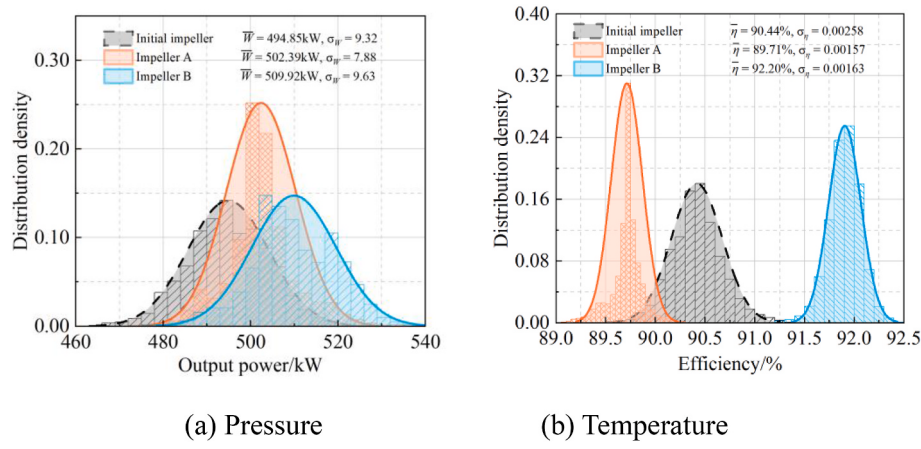


Fig. 23. Comparison of turbine performance uncertainty.

lean angle at the outlet, while impeller B has a smaller one at the outlet.

Fig. 23 shows the performance uncertainty of the selected impellers. As a result of the power optimization, impeller A improves the power by 1.52% compared to the initial impeller, and its standard deviation decreases by 15.45%. Its efficiency robustness is also improved, but the drawback is the decrease in average efficiency. Impeller B not only improves the average efficiency and the efficiency robustness but also increases the average power. The efficiency of impeller B increases by 1.76% (absolute value), and its standard deviation decreases by 36.82%.

Fig. 24 displays the contour map of flow field uncertainty for the selected impellers. Compared with the initial impeller, the uncertainties of the temperature field and pressure field show little variation for impeller A and impeller B. The optimization results reduce the uncertainty in the velocity field. The two sensitive regions on the suction side of the blade with larger FPCV values are reduced in area and merged into one. The results are confirmed again with the detailed statistical FPCV

Table 9
Comparison of field uncertainty through FPCV.

	Pressure		Temperature		Velocity	
	Mean	Max	Mean	Max	Mean	Max
Initial impeller	5.29×10^{-3}	3.71×10^{-2}	3.58×10^{-3}	5.59×10^{-3}	4.78×10^{-2}	3.45×10^{-1}
Impeller A	5.25×10^{-3}	4.07×10^{-2}	3.50×10^{-3}	5.30×10^{-3}	4.23×10^{-2}	3.20×10^{-1}
Impeller B	5.47×10^{-3}	4.30×10^{-2}	3.58×10^{-3}	5.45×10^{-3}	4.30×10^{-2}	3.14×10^{-1}

values listed in Table 9. The mean and maximum FPCV of pressure and temperature fields differ negligibly for the three impellers. It may explain by the fact that the initial pressure and temperature fields are not very sensitive to input uncertainties. Slight differences in the

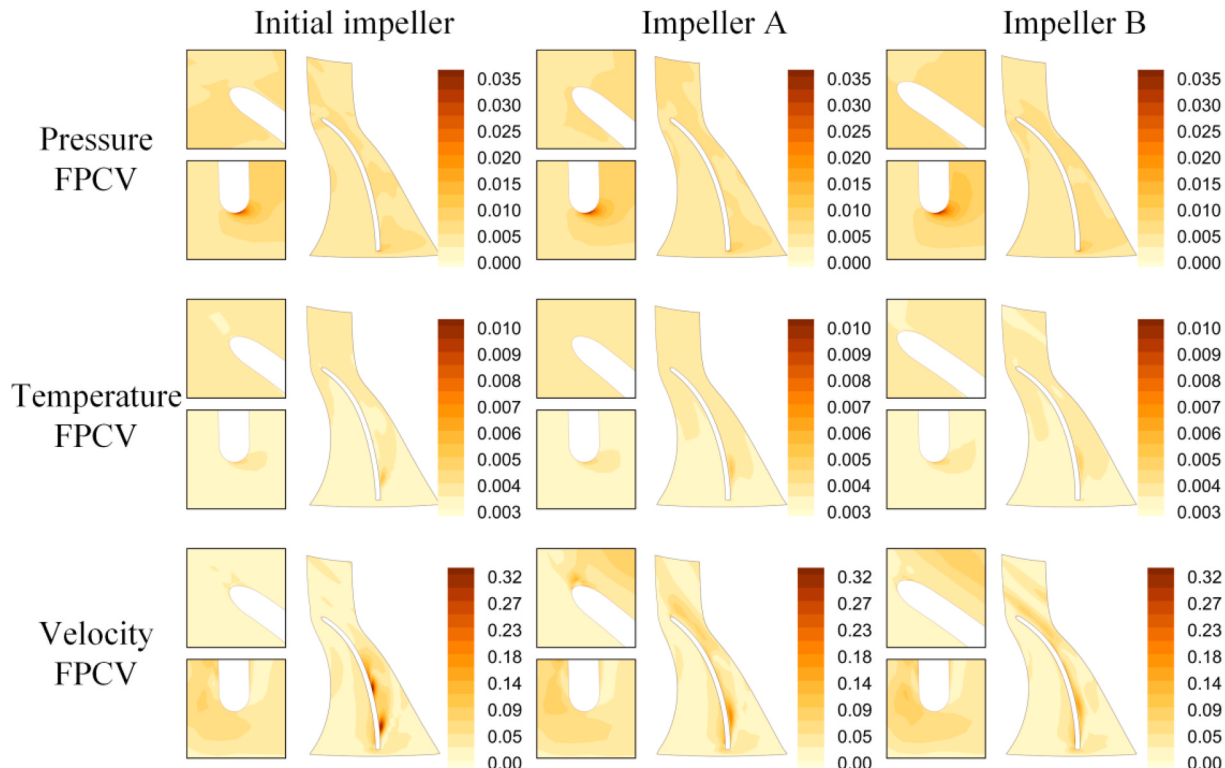


Fig. 24. Comparison of flow fields uncertainty.

number and distribution of grid nodes due to different geometric models may also contribute to this. Significant robustness improvement is achieved in the velocity field, and the mean FPCV of the velocity field decreased by 11.51% and 10.04% for impeller A and impeller B, respectively. The results further demonstrate the improvement of aerodynamic robustness and the feasibility of the proposed framework.

4. Conclusions

In this work, an innovative DGNN model is constructed to assist the uncertainty qualification and aerodynamic robust optimization of turbomachinery. An aerodynamic robust optimization framework that integrates this novel graph learning method is developed. To verify the reliability of our model, a turbine impeller for the solar-based SCO_2 Brayton cycle is considered. The sensitivity of turbine performance and flow fields to multi-source uncertain parameters is analyzed with the help of the proposed model and MC method. The impeller is optimized for two optimization objectives (efficiency robustness and power robustness) by NSGA II. The main conclusions are obtained as follows:

The DGNN model is constructed under the frame of GNNs, which realize the nonlinear mappings of the feature parameters to flow fields and flow fields to aerodynamic performance. The CFD grid information and the adjacency matrix of grids are transformed into graph data. With this innovative approach, CFD flow fields on arbitrary grids can be accurately described and directly used for network training. The precision of the CFD results and the local refinement feature of the mesh are preserved, and pixelation errors are avoided.

The proposed graph learning approach can achieve great regression accuracy. The complex flow phenomena in the turbine can be accurately predicted, and the FMSE of all flow fields is less than 5×10^{-4} for most test samples. Our model is superior to other classical surrogate models on aerodynamic performance prediction. At the same time, it can predict flow fields that cannot be handled by classical surrogate models. The TRE of all performance metrics is less than 0.5% for most samples. The training size analysis shows the proposed model can provide satisfactory results with limited training samples. Moreover, DGNN can provide an almost real-time response for a given input, taking only 0.02 s to obtain the aerodynamic performance and flow fields.

The sensitivity of turbine performance to multi-source uncertainties is analyzed by the proposed DGNN model. The fluctuation of turbine power is mainly driven by thermodynamic uncertainties. The impacts of geometric uncertainty and thermodynamic uncertainties on efficiency are similar and slightly larger than that of rotation speed uncertainty.

Nomenclature

A	Adjacency matrix of grid nodes
B	Bezier curves
d	Number of predefined flow field attributes
E	The set of edges in a graph
e	Edge pointing from one node to another node
f	True flow fields
$\hat{\mathbf{f}}$	Predicted flow fields
G	Mathematical representation of a graph
n	Number of grid vertices
N	Number of samples
P	Pressure [MPa]
r	Rotation speed [rpm]
T	Temperature [K]
t	Tip clearance [mm]
u	Uncertain parameters
V	Velocity [$\text{m} \cdot \text{s}^{-1}$]
V	The set of nodes in a graph
\bar{W}	Mean output power [MW]

Under the coupling effect, the maximum fluctuation ranges are 6.74% and 1.07% for power and efficiency. The uncertain response of flow fields is also obtained. The velocity field is most sensitive to the input uncertainties, while the temperature field is least sensitive.

The optimized result of power robust optimization improves the power by 1.52% and reduces the standard deviation of power by 15.45%. The efficiency robust optimization achieves an efficiency improvement of 1.76% (increment) and an efficiency standard deviation reduction of 36.82%. The effectiveness of the proposed framework for solving aerodynamic robust optimization problems is demonstrated.

Thanks to the powerful nonlinear mapping capability, deep learning methods can be an effective alternative to CFD. It can realize high-precision predictions of complex flow and performance in real-time and assist in designing and optimizing turbomachinery. Future research could focus on improving deep learning models and applying deep learning models to multidisciplinary problems, expecting to provide an effective and general approach for the construction of the digital twin of turbomachinery systems.

Credit author statement

Jinxing Li: Conceptualization, Methodology, Writing- Original draft, Writing- Reviewing and Editing. **Tianyuan Liu:** Conceptualization, Methodology, Software, Writing- Reviewing and Editing. **Guangya Zhu:** Software, Writing- Reviewing and Editing. **Yunzhu Li:** Writing- Reviewing and Editing. **Yonghui Xie:** Conceptualization, Resources, Supervision, Validation.

Declaration of competing interest

The authors declare that they have no known competing financial interests or personal relationships that could have appeared to influence the work reported in this paper.

Data availability

The authors do not have permission to share data.

Acknowledgment

The work was fully supported by National Science and Technology Major Project (J2019-IV-0022-0090).

\mathbf{X}	Node feature matrix of a graph
x	Control point of blade profile
\mathbf{x}	Feature vector
\mathbf{z}	Coordinates of grid vertices
$f(\cdot)$	Activation function
$f_a(\cdot)$	Aggregation function
$\mathcal{N}(\cdot)$	All neighborhoods of a node
$\hat{F}(\cdot)$	Mapping of flow field prediction network
$\hat{Y}(\cdot)$	Mapping of performance discrimination network

Greek symbols

Θ	Input feature parameters
σ	Standard deviation
$\bar{\eta}$	Mean efficiency
ψ	True aerodynamic performance
$\hat{\psi}$	Predicted aerodynamic performance
\mathcal{D}	Predefined dataset by numerical simulations
\mathcal{L}_F	Loss function of flow field prediction network
\mathcal{L}_Y	Loss function of flow field prediction network
Θ_F	Learnable parameters in flow field prediction network
Θ_Y	Learnable parameters in performance discrimination network

Superscripts

l	The index of the network layer
m	The index of fields
s	The index of the performance parameter type

Subscripts

a	Angle
m	Meridional
i, j	The index of nodes
in	Inlet
out	Outlet

Abbreviation

ARO	Aerodynamic robust optimization
CFD	Computational fluid dynamics
CNN	Convolutional neural network
DGNN	Dual graph neural network
FPCV	Field point-wise coefficient of variation
FMSE	Field mean squared error
GPR	Gaussian Process Regression
GNN	Graph neural network
LHS	Latin hypercube sampling
MAE	Mean absolute error
MC	Monte Carlo
NIPC	Non-intrusive polynomial chaos
PR	Polynomial Regression
RMSE	Root mean squared error
RF	Random Forest
SVR	Supported Vector Regression
TRE	Target relative error
UQ	Uncertainty quantification

References

- [1] Lv GC, Yang JG, Shao WY, Wang XF. Aerodynamic design optimization of radial-inflow turbine in supercritical CO₂ cycles using a one-dimensional model. *Energy Convers Manag* 2018;165:827–39.
- [2] Ansarifard N, Kianejad SS, Fleming A, Henderson A, Chai S. Design optimization of a purely radial turbine for operation in the inhalation mode of an oscillating water column. *Renew Energy* 2020;152:540–56.
- [3] Garzon VE, Darmofal DL. Impact of geometric variability on axial compressor performance. *J Turbomach* 2003;125(4):692–703.
- [4] Ghisu T, Shahpar S. Affordable uncertainty quantification for industrial problems: application to aero-engine fans. *J Turbomach* 2018;140(6).
- [5] Schnell R, Lengyel-Kampmann T, Nicke E. On the impact of geometric variability on fan aerodynamic performance, unsteady blade row interaction, and its mechanical characteristics. *J Turbomach* 2014;136(9):1–14.
- [6] Liu Z, Wang X, Kang S. Stochastic performance evaluation of horizontal axis wind turbine blades using non-deterministic CFD simulations. *Energy* 2014;73:126–36.
- [7] Razaaly N, Persico G, Congedo PM. Impact of geometric, operational, and model uncertainties on the non-ideal flow through a supersonic ORC turbine cascade. *Energy* 2019;169:213–27.
- [8] Wang X, Zou Z. Uncertainty analysis of impact of geometric variations on turbine blade performance. *Energy* 2019;176:67–80.
- [9] Xia Z, Luo J, Liu F. Statistical evaluation of performance impact of flow variations for a transonic compressor rotor blade. *Energy* 2019;189.

- [10] Tang X, Gu N, Wang W, Wang Z, Peng R. Aerodynamic robustness optimization and design exploration of centrifugal compressor impeller under uncertainties. *Int J Heat Mass Tran* 2021;180.
- [11] Karimi MS, Raissee M, Salehi S, Hendrick P, Nourbakhsh A. Robust optimization of the NASA C3X gas turbine vane under uncertain operational conditions. *Int J Heat Mass Tran* 2021;164.
- [12] Javed A, Pecnik R, Van Buijtenen JP. Optimization of a centrifugal compressor impeller for robustness to manufacturing uncertainties. *J Eng Gas Turbines Power* 2016;138(11).
- [13] Tang X, Wang Z, Xiao P, Peng R, Liu X. Uncertainty quantification based optimization of centrifugal compressor impeller for aerodynamic robustness under stochastic operational conditions. *Energy* 2020;195.
- [14] Ji Y, Liu Y, Jiang W, Zhang C. Aerodynamic analysis and design optimization of a centrifugal compressor impeller considering realistic manufacturing uncertainties. *Aero Sci Technol* 2021;115.
- [15] Huang R, Zhang Z, Zhang W, Mou J, Zhou P, Wang Y. Energy performance prediction of the centrifugal pumps by using a hybrid neural network. *Energy* 2020;213.
- [16] Rossi M, Renzi M. A general methodology for performance prediction of pumps-as-turbines using Artificial Neural Networks. *Renew Energy* 2018;128:265–74.
- [17] Kadhim HT, Rona A. Design optimization workflow and performance analysis for contoured endwalls of axial turbines. *Energy* 2018;149:875–89.
- [18] Shi D, Liu T, Xie Y, Zhang D. Design and Optimization of an S-CO₂ Turbine Based on Gauss Process Regression. *J Chin Soc Power Eng Energy* 2019;39(11):876–83.
- [19] Fast M, Assadi M, De S. Development and multi-utility of an ANN model for an industrial gas turbine. *Appl Energy* 2009;86(1):9–17.
- [20] Liu Z, Karimi IA. Gas turbine performance prediction via machine learning. *Energy* 2020;192.
- [21] Huang M, Li Z, Li J. Investigations on the aero-thermal performance of the turbine blade winglet squealer tip within an uncertainty framework. *Aero Sci Technol* 2022;123.
- [22] Hou CKJ, Behdinan K. Dimensionality reduction in surrogate modeling: a review of combined methods. *Data Science and Engineering* 2022;7(4):402–27.
- [23] Sun L, Liu T, Xie Y, Zhang D, Xia X. Real-time power prediction approach for turbine using deep learning techniques. *Energy* 2021;233.
- [24] Qiuwan D, Like Y, Li L, Liu T, Di Z. Aerodynamic design and optimization of blade end wall profile of turbomachinery based on series convolutional neural network. *Energy* 2022;244:122617.
- [25] Xie Y, Liu T, Zhang D. Intelligent steam turbine and its advances under new energy circumstance. *Proc Chin Soc Electr Eng* 2021;41(2):394–408.
- [26] Brunton SL, Nathan Kutz J, Manohar K, Aravkin AY, Morgansen K, Klemisch J, et al. Data-driven aerospace engineering: reframing the industry with machine learning. *AIAA J* 2021;1–26.
- [27] Jin X, Cheng P, Chen W-L, Li H. Prediction model of velocity field around circular cylinder over various Reynolds numbers by fusion convolutional neural networks based on pressure on the cylinder. *Phys Fluids* 2018;30(4).
- [28] Liu T, Li Y, Jing Q, Xie Y, Zhang D. Supervised learning method for the physical field reconstruction in a nanofluid heat transfer problem. *Int J Heat Mass Tran* 2021;165.
- [29] Li Y, Liu T, Wang Y, Xie Y. Deep learning based real-time energy extraction system modeling for flapping foil. *Energy* 2022;246.
- [30] Lee S, You D. Data-driven prediction of unsteady flow over a circular cylinder using deep learning. *J Fluid Mech* 2019;879:217–54.
- [31] Yang L, Wang Q, Rao Y. Searching for irregular pin-fin shapes for high temperature applications using deep learning methods. *Int J Therm Sci* 2021;161.
- [32] Guo D, Liu T, Zhang D, Xie Y. Fast reconstruction method of the stress field for the steam turbine rotor based on deep fully convolutional network. *J Eng Gas Turbines Power* 2021;144(2).
- [33] Jiang H, Nie Z, Yeo R, Farimani AB, Kara LB. StressGAN: a generative deep learning model for two-dimensional stress distribution prediction. *J Appl Mech* 2021;88(5).
- [34] Han R, Wang Y, Zhang Y, Chen G. A novel spatial-temporal prediction method for unsteady wake flows based on hybrid deep neural network. *Phys Fluids* 2019;31(12).
- [35] Sekar V, Jiang Q, Shu C, Khoo BC. Fast flow field prediction over airfoils using deep learning approach. *Phys Fluids* 2019;31(5).
- [36] Kashefi A, Rempe D, Guibas LJ. A point-cloud deep learning framework for prediction of fluid flow fields on irregular geometries. *Phys Fluids* 2021;33(2).
- [37] Wang Y, Liu T, Zhang D, Xie Y. Dual-convolutional neural network based aerodynamic prediction and multi-objective optimization of a compact turbine rotor. *Aero Sci Technol* 2021;116.
- [38] Asif NA, Sarker Y, Chakraborty RK, Ryan MJ, Ahamed MH, Saha DK, et al. Graph neural networks: a comprehensive review on non-euclidean space. *IEEE Access* 2021;9:60588–606.
- [39] Zheng C, Fan X, Wang C, Qi J, GMAN: A graph multi-attention network for traffic prediction. 34th AAAI conference on artificial intelligence. AAAI; 2020. p. 1234–41.
- [40] Mansimov E, Mahmood O, Kang S, Cho K. Molecular geometry prediction using a deep generative graph neural network. *Sci Rep* 2019;9(1):20381.
- [41] Fan W, Ma Y, Li Q, He Y, Zhao E, Tang J, et al. Graph neural networks for social recommendation. The World Wide Web Conference on - WWW '192019. p. 417–426.
- [42] Li Z, Farimani AB. Graph neural network-accelerated Lagrangian fluid simulation. *Comput Graph* 2022;103:201–11.
- [43] Sanchez-Gonzalez A, Godwin J, Pfaff T, Ying R, Leskovec J, Battaglia PW. Learning to simulate complex physics with graph networks. 37th International Conference on Machine Learning, ICML 2020;PartF168147-11:8428–37.
- [44] Pfaff T, Fortunato M, Sanchez-Gonzalez A, Battaglia PW. Learning mesh-based simulation with graph networks. 2020.
- [45] Xu M, Song S, Sun X, Zhang W. A convolutional strategy on unstructured mesh for the adjoint vector modeling. *Phys Fluids* 2021;33(3).
- [46] Li J, Liu T, Wang Y, Xie Y. Integrated graph deep learning framework for flow field reconstruction and performance prediction of turbomachinery. *Energy* 2022;254:124440.
- [47] Zhou J, Cui G, Hu S, Zhang Z, Yang C, Liu Z, et al. Graph neural networks: a review of methods and applications. *AI Open* 2020;1:57–81.
- [48] Hamilton WL, Ying R, Leskovec J. Inductive representation learning on large graphs, vol. 30. Long Beach, CA: 31st Annual Conference on Neural Information Processing Systems (NIPS); 2017.
- [49] Hendrycks D, Gimpel K. Gaussian error linear units. GELUs; 2016, 08415. arXiv: 1606.
- [50] Gao H, Ji S. Graph U-Nets 2019;05178. arXiv:1905.
- [51] Paszke A, Gross S, Massa F, Lerer A, Bradbury J, Chanan G, et al. PyTorch: an imperative style, high-performance deep learning library, vol. 32. Vancouver, CANADA: 33rd Conference on Neural Information Processing Systems (NeurIPS); 2019.
- [52] Kingma DP, Ba J. Adam: a method for stochastic optimization. 2014. arXiv: 1412.6980.
- [53] Fey M, Lenssen JE. Fast graph representation learning with PyTorch geometric. 2019. arXiv:1903.02428.
- [54] Pedregosa F, Varoquaux G, Gramfort A, Michel V, Thirion B, Grisel O, et al. Scikit-learn: machine learning in Python. *J Mach Learn Res* 2011;12:2825–30.